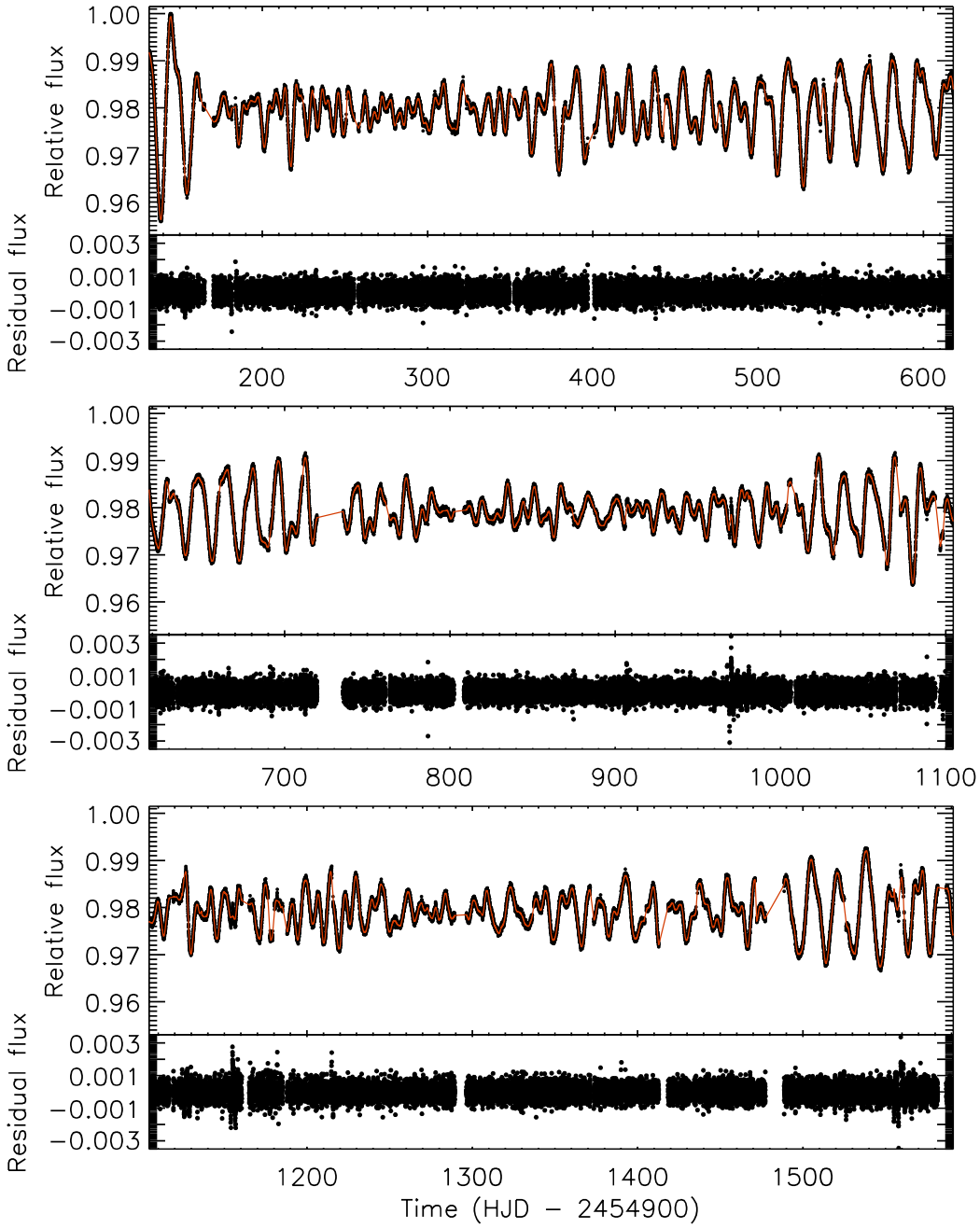

Fig. 8. Upper panels: The PDC light curve of Kepler-30 (solid black dots) and the unregularized best fit obtained with our spot model (red solid line). Lower panels: the residuals of the best fit.

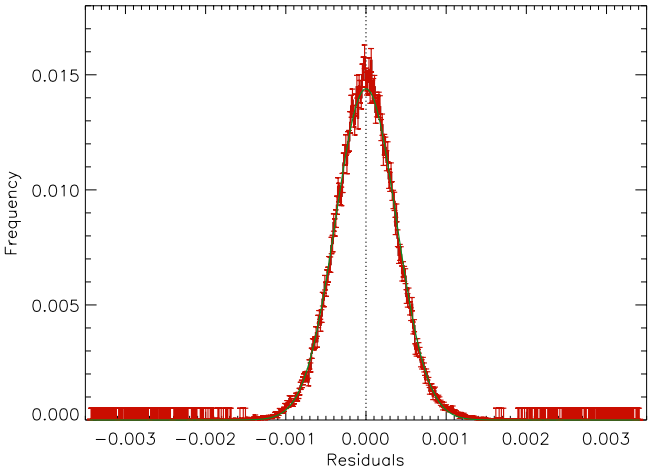

Fig. 9. Distribution of the residuals of the unregularized best fit to the PDC light curve in Fig. 8.

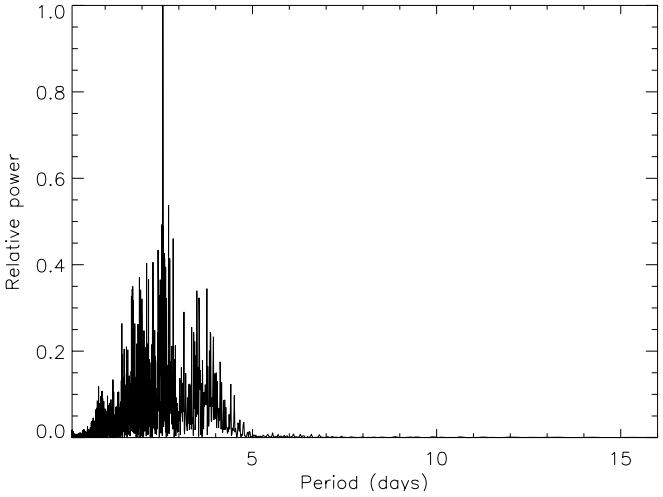

Fig. 10. GLS periodogram of the residuals of the unregularized best fit to the PDC light curve in Fig. 8.

modulation in the total spotted area of Kepler-30, reminiscent of the short-term cycles found in CoRoT-2 (Lanza et al. 2009; Zaqarashvili et al. 2021).

Such a short-term cycle of ∼34 days is virtually close to the synodic period $P_{\rm syn}$ = 35.2 days of the planet Kepler-30b as computed with a rotation period $P_{\rm rot}$ = 16.0 days and an orbital period $P_{\rm orb}$ = 29.334 days from $P_{\rm syn}^{-1} = P_{\rm rot}^{-1} - P_{\rm orb}^{-1}$. This period also appears in the periodogram of Fig. 6 and is close to the period of the modulation of the spotted area. In addition, the 23.1-day period (see Fig. 6) is close to the synodic period of Kepler-30c. However, an interpretation in terms of tidal or magnetic star-planet interactions (cf. Lanza 2012, 2013) is problematic because of the large star-planet separations that range from ∼ 42 to ∼ 121 stellar radii for the three planets (see http://exoplanets.org). More precisely, both the tidal torque on the star and the energy density of its coronal magnetic field decrease with distance as $(a/R_{\rm s})^{-6}$, where a is the orbital separation and $R_{\rm s}$ the radius of the star.

7.3. Multiscale multifractal analysis

7.3.1. Fluctuation functions

In Figs. 13 and 14, we plot the fluctuation functions $F_q(n)$ vs. the timescale n for different values of q for the PDC and SAP timeseries, respectively. In this logarithmic plot, the scaling relation given by equation (6) becomes a straight line in the intervals of n where $h(q)$ is constant. A value of n separating two consecutive intervals where $h(q)$ is constant for a given q is called a *crossover*. We see a crossover in the plots for the values of $q > 0$ at 8.7 days as indicated by the vertical dashed line. The crossover corresponds to the optimal delay time as determined with the procedure described in Section 6.1 (cf. Fig. 7). The change in slope is made clear by the green dashed line that gives an average slope $H = h(2) = 0.95$ for timescales shorter than 8.7 days. The small decrease in the fluctuation functions following the crossover and extending up to the rotation period of 16.8 days is barely significant and is due to the variation in amplitude produced by the use of a moving average to approximate what is actually a nearly sinusoidal modulation in the computation of the fluctuation function itself (see Appendix A). Once the rotation period is reached, the amplitude of the fluctuation function saturates at a nearly constant value, except for some small oscillations produced by the sinusoidal modulation of the signal (cf. Appendix B). In other words, the slope h beyond the crossover is virtually zero because the variability due to the rotational modulation dominates over the stochastic fluctuations. We remind that the fluctuation function with $q = 2$ is based on the variance of the fluctuations in the time series.

For both the PDC and SAP timeseries, we find a crossover at the timescale corresponding to the first harmonic of the rotation period, i.e., ∼ 8.7 days. The predominance of the modulation at the first harmonic is seen in the light curves of active stars when two active longitudes on opposite hemispheres are responsible for most of the flux modulation, a behaviour that is confirmed by our spot modelling (see Sect. 7.2). From the perspective of stochastic process analysis, the behaviour we see is reminiscent of an attractor (see Figure 7) with a phase trajectory that revolves around a period-one fixed point. As a result, the logarithms of the fluctuation functions $F_q(n)$ show a linear regime until ∼8.7 days after which they get saturated and start weakly oscillating. There is a slight difference in the level of oscillation when the time series PDC and SAP are compared as can be seen in Figures 13 and 14. Based on the results in Sect. 7.1, the presence of a few larger residuals found in the SAP time series probably explains the plateau within the range from 8.7 to 16.8 days, since the noise is responsible for dampening the oscillation.

In Fig. 15, we plot the fluctuation functions for the difference time series RTS. In this case, we see a crossover at a longer timescale of ∼ 23.5 days. We can associate it with the characteristic evolutionary timescales of active regions in Kepler-30 because the rotational modulation was remarkably reduced by subtracting the two timeseries from each other (cf. Sect. 7.2). We remind that the intrinsic variability on timescales longer than 15 − 20 days was preserved in the SAP timeseries, while it was strongly reduced in the PDC timeseries owing to the de-trending applied by the Kepler pipeline (cf. Sect. 3). Therefore, the long-term intrinsic variability stands out in the difference timeseries.

The fluctuation functions of the timeseries of the residuals of the unregularized spot modelling of the PDC light curve are plotted in Fig. 16. We see two crossover at ∼ 1 and ∼ 35 days, where the Hurst exponent $H = h(2)$ changes from 0.73 to 0.10 and then to 0.37, respectively. Therefore, the fluctuations with timescales shorter than ∼ 1 day are characterized by persistence,

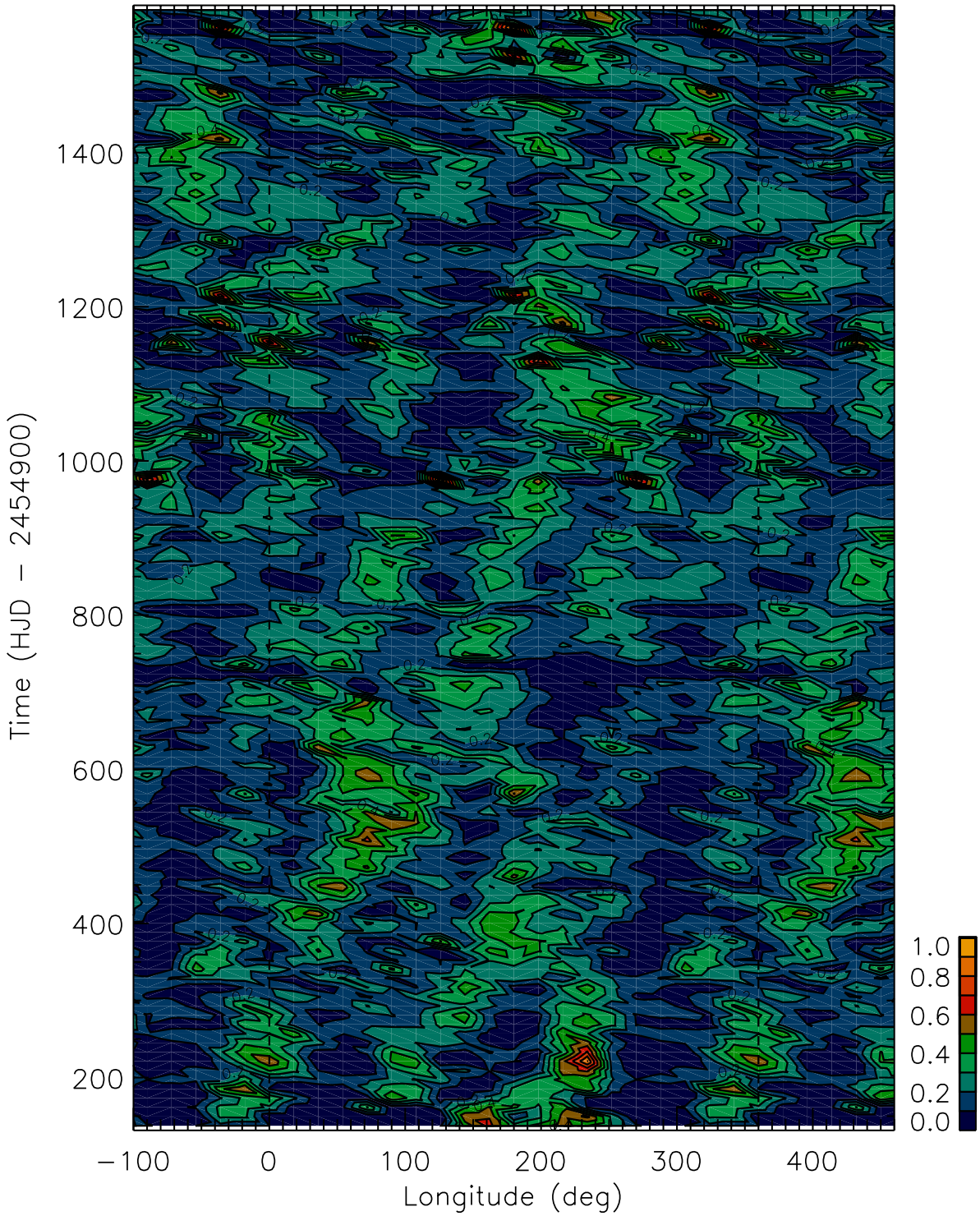

Fig. 11. Distribution of the spot filling factor vs. the longitude and time for the ME regularized spot model of the PDC light curve of Kepler-30. The minimum of the filling factor corresponds to dark blue regions, while the maximum is rendered in orange (see the colour scale close to the lower right corner of the plot). Note that the longitude scale of the horizontal axis is extended beyond the $[0°, 360°]$ interval to better follow the migration of the starspots.

while those on longer timescales show a value of H characteristic of antipersistent time series. The timescale of $\sim$ 1 day is characterized by a remarkable increase of the power level in the GLS power spectrum of the residuals (cf. Fig. 10) and the multifractal analysis reveals a change in the persistence property of the fluctuations just at that timescale. It corresponds to the characteristic turnover time of supergranular convective cells in the Sun and Sun-like stars (cf. Meunier et al. 2015). The other crossover at $\sim$ 35 days coincides with the possible short-term cycle in the area of the starspots (cf. Sect. 7.2) and the change in the slope of the fluctuation functions may indicate changes in the properties of convection at that timescale of stellar activity. The fluctuations functions of the spot model residuals of the SAP lightcurve are very similar and shall not be discussed here. In both the cases,

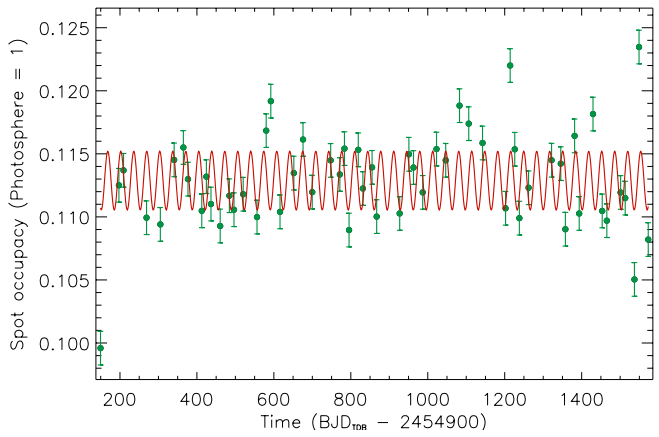

Fig. 12. The total spotted area on Kepler-30 as derived from the spot modelling of the PDC light curve vs. the time (green dots). A sinusoid with a period of 33.784 days corresponding to the maximum of the GLS periodogram is overplotted (red solid line).

we do not find any particular feature of the fluctuation functions at the peak period of 2.565 days in the GLS periodogram of the residuals, suggesting that it is not significant and not associated with a change in the behaviour of the stellar light fluctuations.

We based our conclusions on the fluctuation functions $F_q(n)$ with positive q where the effect of large-scale fluctuations is amplified with respect to that of small-scale fluctuations in the computation of the moments of order $q > 0$. Conversely, small-scale fluctuations will have the most important impact on the fluctuation functions $F_q(n)$ when $q < 0$ because the effect of large-scale fluctuations is attenuated by a negative exponent in the calculation of the momenta (cf. eq. A.5). In all the above plots of the fluctuation functions $F_q(n)$ with $q < 0$, we see that the exponent of the scaling law, that is, the slope of the plot, changes frequently and abruptly. This indicates that the asymptotic regime where $F_q(n) \propto n^{h(q)}$ is not fully reached in those plots likely as an effect of a few very small fluctuations that dominate the functions.

7.3.2. Hurst exponent surfaces

Now, we pass to investigate the effects of a periodic trend using the Hurst surface $h(q, \tau)$. With this, we can study the generalized Hurst exponent h behaviour not only as a function of the q-moment (standard MFDMA method) but also as a function of the timescale τ (MFDMAτ). The Hurst surfaces illustrated in Figs. 17, 18 and 19 calculated for PDC, SAP and RTS data show abundant features to analyse, which may be hidden by the standard MFDMA proposed by Gu & Zhou (2010).

For a fixed scale n, when q changes from −5 to 5, there are downward trends for all $h(q, \tau)$ surfaces, except in the domain where $n < 8.7$ ($n < 23.5$) days and $q < 0$ for PDC and SAP (RTS) series. In particular, we can recover the results from the standard MFDMA method, calculating the scaling exponent for each q at the whole scale range n. In this way, varying q, when τ changes from small to large values, all curves of $h(q > 0, \tau)$ show a rapid rise to their peak values, then become more or less constant showing a plateau. However, for $h(q < 0, \tau)$, there are oscillations that increase with the increase of $|q|$, in addition to a stronger jump when τ is small and $q < 0$ for PDC and SAP and less pronounced for RTS. The presence of bumps at negative q values in the Hurst surfaces in Figs. 17, 18 and 19 may be the results of the amplified impact of small fluctuations that in turn depends on several effects such as the evolution of active regions and the differential rotation.

The main feature of the $h(t, \tau)$ plots is the remarkable decrease of the value of h from ≈ 1 for $q \sim -5$ to ~ 0.5 for $q > 0$. This suggests that the small scale fluctuations, the effect of which on h is amplified for $q < 0$, have a strong degree of persistence, while the large scale fluctuations, which dominate h for $q > 0$ are more similar to an uncorrelated random process. The results based on the portion of the plots with $q < 0$ should be taken with some caution because of the sizeable fluctuations of h, but these plots suggest a different physical origin for small and large scale fluctuations in the Kepler-30 light curve, a conclusion that can be useful to constrain models of stellar microvariability. Crossovers are not clearly evident in the $h(t, \tau)$ plots of the SAP and PDC timeseries, except for that at $\tau = 8.7$ days already discussed above. This happens probably because the variability is dominated by the rotational modulation. Therefore the SAP and PDC $h(t, \tau)$ surfaces show only a tiny hint of possible slope changes for τ between ≈ 20 and ≈ 35 days that could be associated with the evolution of active regions. On the other hand, the $h(t, \tau)$ plot of the RTS timeseries shows a clear crossover at ~ 23 days that extends over an interval of q and that is likely indicating the typical active regions evolution timescale as estimated from the spot modelling.

Following the discussion in Sect. 5.2 and in de Freitas et al. (2017), we computed the $\langle S_{\rm ph} \rangle_{k=5}$ activity index for Kepler-30 finding 4712 and 5209 parts per million for the PDC and SAP pipelines, respectively. The larger value found with the SAP data is a consequence of the reduction of the stellar variability in the PDC timeseries for timescales longer than $\sim$ 15 days. The Hurst exponent surface $h(2, \tau)$ shows a steep increase up to $\tau = 8.7$ days followed by an almost constant plateau, indicating that most of the variability in the timeseries of Kepler-30 occurs for timescales shorter than half the rotation period of the star which corresponds to only 10% of the time interval sampled by the $\langle S_{\rm ph} \rangle_{k=5}$ index. Therefore, such an index provides a very limited description of the light variability in the case of Kepler-30, while the Hurst exponent surfaces allow a detailed description of the dependence of the variability on the timescale. The short-term spot cycle of $\sim$ 34 days of Kepler-30 has a period shorter that the five rotations adopted to compute the $\langle S_{\rm ph} \rangle_{k=5}$ index, therefore this index may not be appropriate to sample the activity timescales characteristic of Kepler-30.

7.3.3. Effect on surrogate time series

As mentioned in Sect. 5.2, multifractality can have two sources: long-term correlations or a fat-tailed probability distribution of the fluctuations. In the case of Kepler time series, it was already shown that the first source of multifractality is by far the dominant one (de Freitas et al. 2017).

We confirm this result in the specific case of Kepler-30 by calculating $h(q, \tau)$ for the shuffled and phase-randomized surrogates of the three timeseries considered above.

Figure 20 shows the average results of 200 realizations of the shuffled and phase-randomized surrogates of PDC (upper panels), SAP (middle panels) and RTS (bottom panels). In fact, as can be seen in Fig. 20, the shuffling procedure destroyed the correlations, i.e., the Hurst surface $h(q, \tau)$ is flat ($\langle h(q, \tau) \approx 0.5 \rangle$, the value of h corresponding to white noise). However, the Hurst surface of phase-randomized series vary slightly both with the order q and timescale τ ($\langle h(q, \tau) \approx 0.82 \rangle$). These findings suggest that

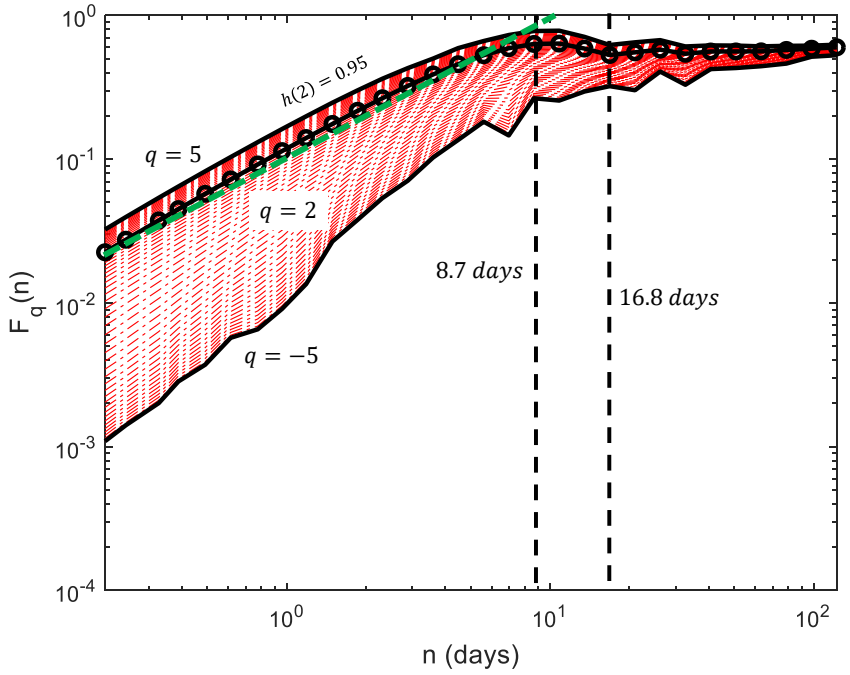

Fig. 13. The log-log plot of the fluctuation functions $F_q(n)$ (black circle for $q = 2$) calculated for the final PDC time series presented in Fig. 5. The red curves correspond to q between −5 and 5 in steps of 0.2. Vertical dashed lines mark three domains of the fitting windows for the small n between 29.4 min and 8.7 days, for middle n between 8.7 and 16.8 days and, for the large n greater than 16.8 days. The green dashed line gives the average slope $H = h(2) = 0.95$ for timescales shorter than 8.7 days.

the multifractality of rotational modulation is due to both long-range correlation and non-linearity due to fat-tailed probability distributions, but long-range correlations are the main source of multifractality, which is consistent with the results of standard MFDMA.

8. Summary and Conclusions

In this study, we analysed the rotation and the evolution of photospheric active regions of the moderately young Sun-like star Kepler-30 accompanied by a three-planet system, using both its PDC and SAP timeseries by means of an MFDMA-based multifractality analysis approach in a standard and a new multiscale version. In the latter case, the PDC and SAP timeseries, as well as the difference RTS data, are examined considering the generalized dependence of the local Hurst exponent on the timescale τ by means of the surface $h(q, \tau)$. We also consider the impact of the rotational modulation on the characterization of the multifractal properties of the light fluctuations, as already investigated by de Freitas et al. (2013b, 2016, 2017, 2019a,b), and show that such an impact depends on the timescale. Furthermore, we applied a maximum entropy spot modelling to extract information on the longitude, the area variation, and the evolutionary timescales of the active regions responsible for the rotational modulation of the stellar flux. Such an approach reveals that the characteristic timescales of stellar activity in Kepler-30 are significantly shorter than the five rotations adopted to compute the $\langle S_{\rm ph}\rangle_{k=5}$ index as defined by Mathur et al. (2014), therefore such an index is of limited use to characterize the activity of our target.

Our main conclusions can be summarized as follows:

(i) The fluctuation functions $F_q(n)$ show that the multifractal properties of the Kepler-30 timeseries have a relationship with the range of scale n and, therefore, indicate the limitation of the standard MFDMA method using a fixed timescale. Then, we systematically investigate the dynamic behaviours of the three timeseries, PDC, SAP and RTS, by applying a new approach here named MFDMAτ;

(ii) The Hurst surfaces reveal that for negative q values there are remarkable fluctuations in the local Hurst exponent $h(q, \tau)$ and significant differences for different values of q. Conversely, the positive q values show that the Hurst surfaces become flat starting from a minimum period ($\sim$ 8.7 days) that corresponds to the first harmonic of the rotation period as found by the Lomb–Scargle periodogram in the case of the SAP and PDC timeseries, while it corresponds to the evolutionary timescale of active regions ($\sim$ 23.5 days) for the RTS timeseries, in which the rotational modulation has been almost completely removed. The analysis of the residuals of the spot modelling shows a crossover at $\sim$ 1 day, that coincides with the characteristic turnover time of the supergranules (cf. Sect. 7.3.1), and another at $\sim$ 35 days that corresponds to an increase in the power level of the light fluctuations and a possible short-term cycle in the total area of the starspots (see below), respectively.

(iii) The multifractality of the Kepler-30 time series is principally due to the long-range correlations with a minor contribution from a broad non-Gaussian probability density distribution of the fluctuations. This result is found by comparing the original time series with their shuffled and phase-randomized surrogates. Our $h(t, \tau)$ plots suggest also that the small scale fluctuations that dominate the function F_q for $q < 0$ have a remarkable persistence, while the large scale fluctuations dominating for $q > 0$ have a random and uncorrelated behaviour similar to that of a white noise, once the effect of the rotational modulation has been removed;

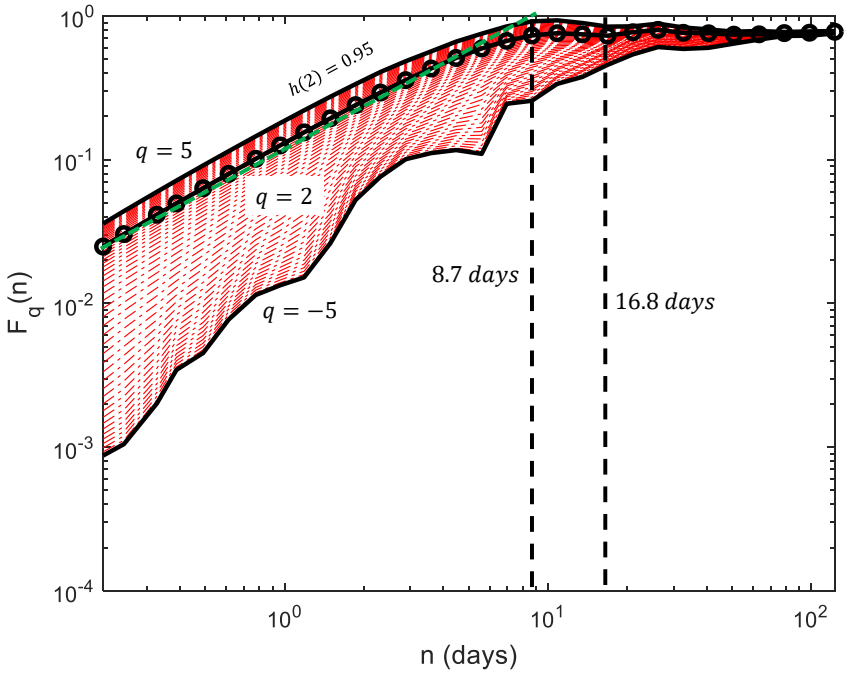

Fig. 14. Idem Figure 13 for final SAP time series.

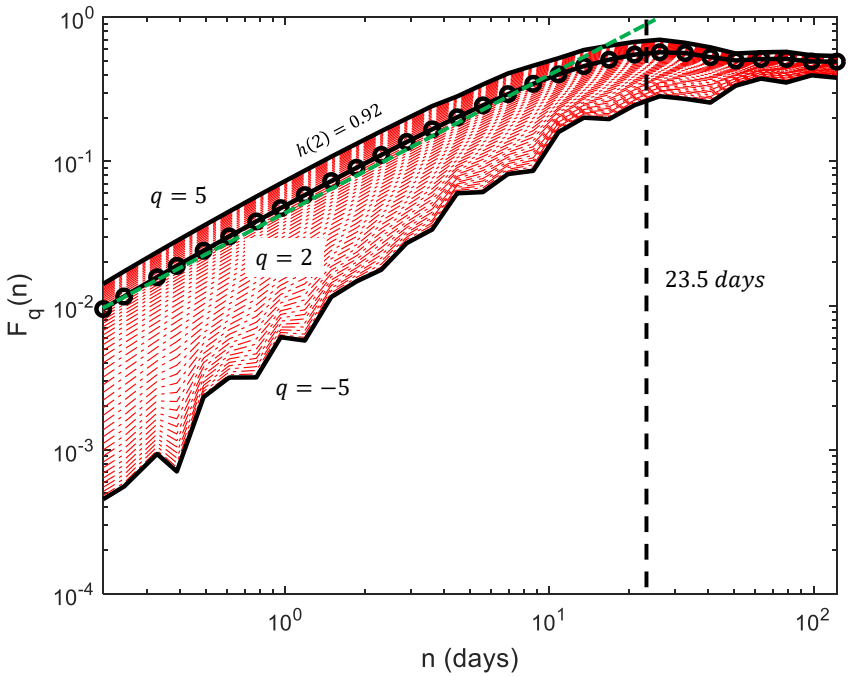

Fig. 15. Idem Figure 13 for final RTS time series. In this case, only two domain are considered and separated by the vertical dashed line at 23.5 days.

(iv) A maximum entropy spot modelling shows that the photospheric features of Kepler-30 evolve on timescales ranging from 10 – 20 days for individual active regions up to a few hundreds of days for the longer-lived active longitudes. Their migration can be used to estimate a lower limit for the relative surface shear of $\Delta\Omega/\Omega \sim 0.02 \pm 0.01$ that should be taken with great caution owing to the rapid evolution of the individual starspots that can mimic the effects attributed to differential rotation. A short-term cycle of about $\sim$ 34 days in the total area of the starspots could be present and its timescale compares well with that found in the difference RTS timeseries as well as with a crossover (a slope change) in the fluctuation functions of the residuals of the spot modelling.

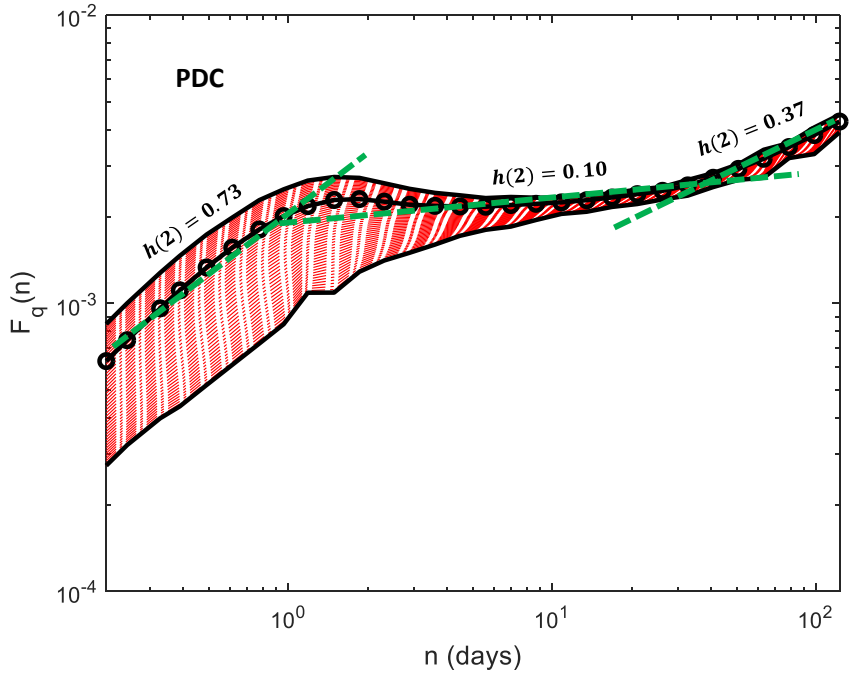

Fig. 16. Fluctuation functions of the residuals of the unregularized spot model of the PDC light curve of Kepler-30.

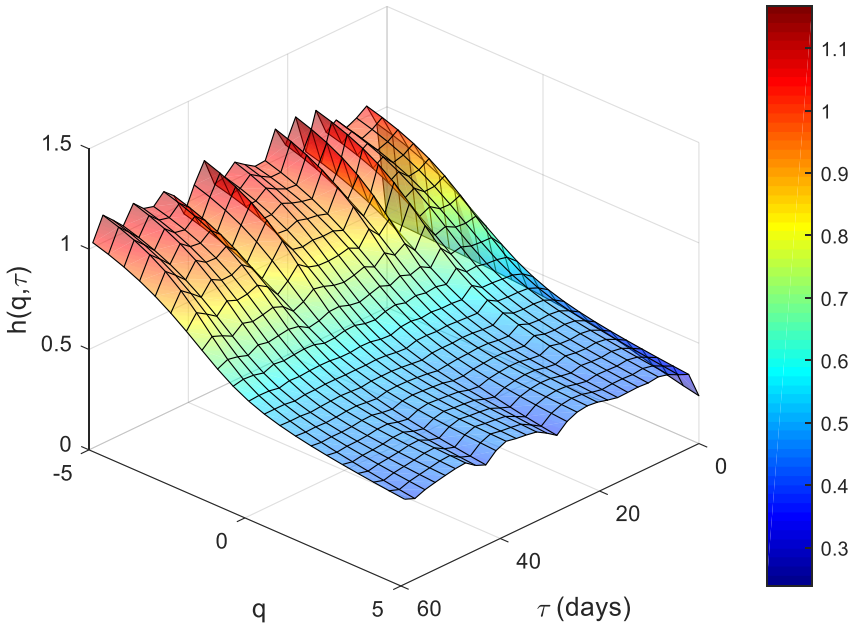

Fig. 17. Hurst surface $h(q, \tau)$ calculated for final PDC time series. The $(h, q)-$plane corresponds to $h(q)$ calculated with the standard MFDMA method. Colorbar indicates values of $h(q, \tau)$, where for $q < 0$ the higher values are found and, for $q > 0$ the lower ones.

(v) Finally, we note a coincidental proximity of some activity timescales with the synodic periods of the two closest planets. The short-term spot cycle of ∼34 days is close to the synodic period of 35.2 days of the planet Kepler-30b when a mean rotation period of 16 days is adopted for Kepler-30. From the Lomb-Scargle periodogram of the RTS time series, a 23.1-day period emerges, that is close to the synodic period of Kepler-30c of 22 days. This period also appears in the multifractal analysis as a crossover of the fluctuation functions and is likely associated with the characteristic evolutionary timescales of active regions in Kepler-30 as indicated by the spot modelling. For the most distant planet Kepler-30d, we did not identify any similar coincidence. Nevertheless, the large separations of planets b and c suggest a great caution in the attribution of such coincidences

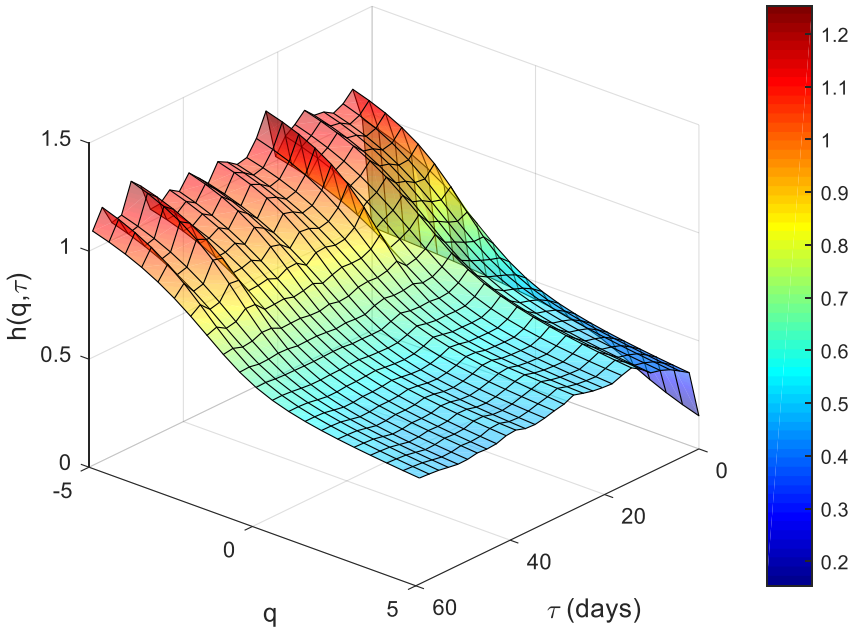

Fig. 18. Idem Figure 17 for SAP data.

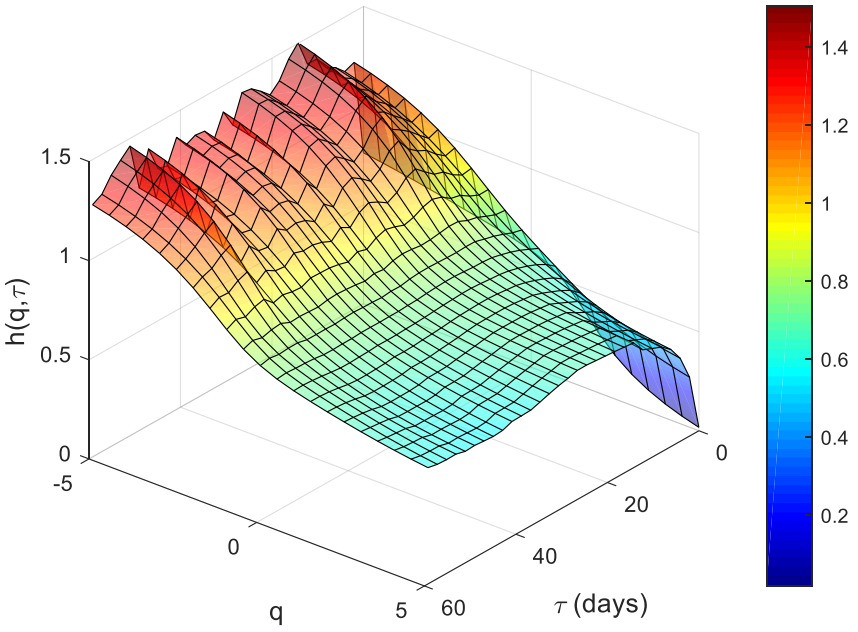

Fig. 19. Idem Figure 17 for RTS data. In this case, random walk-type fluctuations ($H > 1$) are stronger than PDC and SAP data, indicating more apparent slow evolving fluctuations in regime $q < 0$.

to a possible star-planet magnetic interaction (see Sect. 7.2 for more detail).

We pointed out the relevant timescales and the persistence characteristics of the light fluctuations of Kepler-30, an active Sun-like star. This information can provide constraints for the models of the stellar flux variations based on the effects of magnetic fields and surface convection, thus promising to contribute to the refinement of those models in future investigations.

As a perspective, our multifractal methods are particularly interesting for analysing ongoing TESS and future PLATO high-precision photometric timeseries. They represent a useful complement to regularized spot models that can be used for an investigation of the activity phenomena on timescales compara-

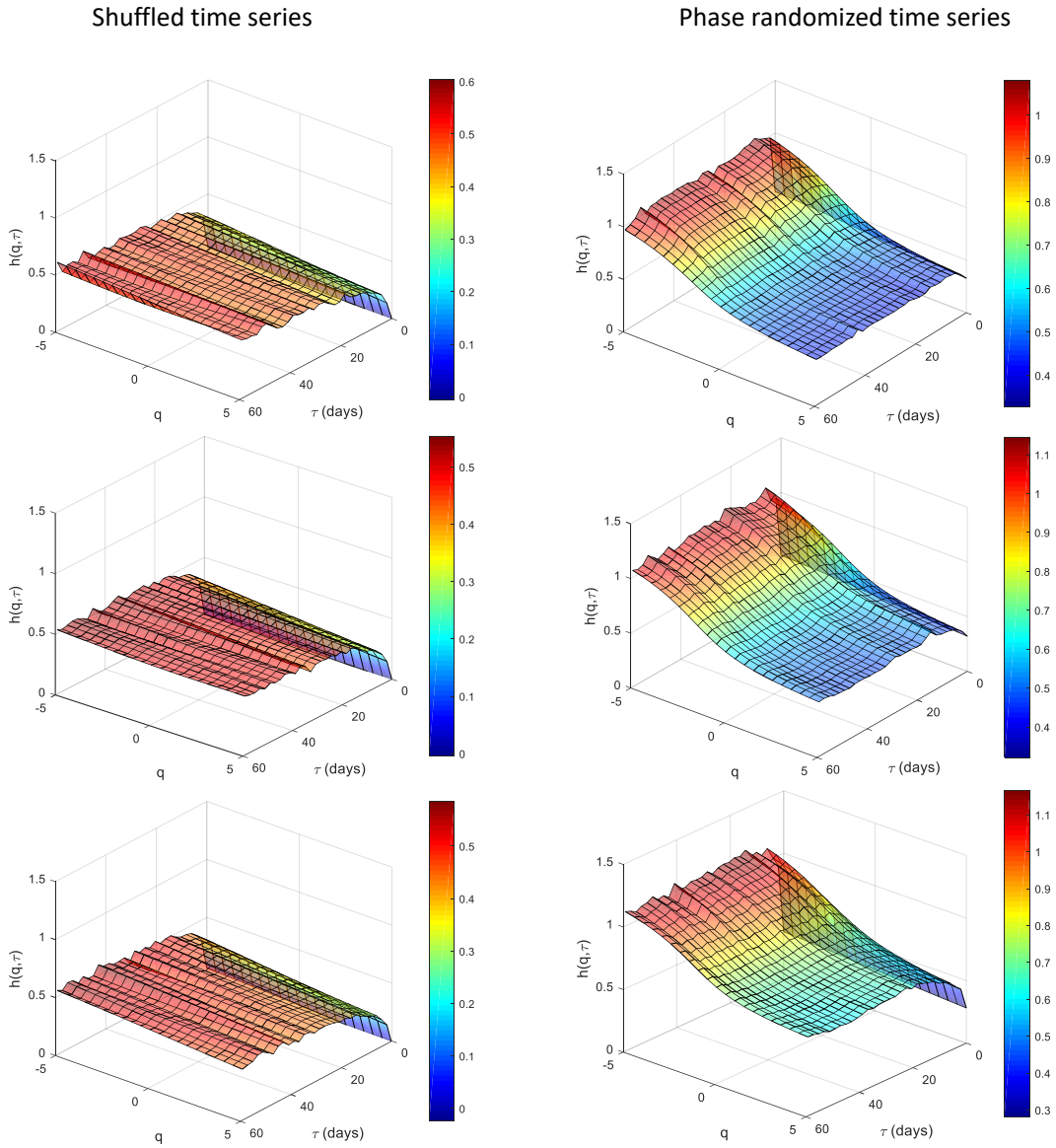

Fig. 20. Hurst surface $h(q, \tau)$ calculated for the shuffled (left side) and phase randomized (right side) versions of time series: PDC (top), SAP (middle) and RTS (bottom). Presented are results averaged over 200 realizations of the surrogate series.

ble with the stellar rotation period or longer, while multi-fractal methods can cover the full range of timescales and characterize the persistence of the fluctuations produced by magnetoconvection on timescales remarkably shorter than the rotation period which are not accessible to spot modelling. On the other hand, we have illustrated how the two methodologies provide comparable results in the range of timescales they have in common. In this case, spot modelling allows us to gain more physical insight on the origin of the characteristic timescales pointed out by the multifractal analysis, at least when they can be associated with starspot evolution or activity cycles. To reduce the degeneracies of spot modelling, it is advisable to target stars whose spin axis inclination can be constrained through the occultations of spots during planetary transits such as in the case of Kepler-30 (Sanchis-Ojeda et al. 2012) or by means of asteroseismology (e.g., Ballot et al. 2006).

Acknowledgements. The authors are grateful to an anonymous referee for a careful reading of the manuscript and several valuable suggestions that helped them to improve their work. DBdeF acknowledges financial support from the Brazilian agency CNPq-PQ2 (grant No. 311578/2018-7). Research activities of STELLAR TEAM of Federal University of Ceará are supported by continuous grants from the Brazilian agency CNPq. AFL gratefully acknowledges support from the INAF Mainstream Project entitled "Stellar evolution and asteroseismology in the context of PLATO space mission" coordinated by Dr. Santi Cassisi. This paper includes data collected by the *Kepler* mission. Funding for the *Kepler* mission is provided by the NASA Science Mission directorate. All data presented in this paper were obtained from the Mikulski Archive for Space Telescopes (MAST). The authors would like to dedicate this paper to all the victims of the COVID-19 pandemic around the world.

References

Agarwal, S., Del Sordo, F., & Wettlaufer, J. S. 2017, AJ, 153, 12
Ballot, J., García, R. A., & Lambert, P. 2006, MNRAS, 369, 1281. doi:10.1111/j.1365-2966.2006.10375.x
Basri, G. & Shah, R. 2020, ApJ, 901, 14
Belete A. B., Bravo J. P., Canto Martins B. L., Leão I. C., De Araújo J. M., De Medeiros J. R., 2018, MNRAS, 478, 3976
Bonomo, A. S., & Lanza, A. F. 2012, A&A, 547, A37

Collier Cameron, A. 2018, Handbook of Exoplanets, H. Deeg & J. A. Belmonte (Eds.), Springer Nature, Switzerland, vol. 3, pp. 1791-1800; doi:10.1007/978-3-319-55333-7_23
De Medeiros, J. R., Lopes, C. E. F., Leão, I. C., et al. 2013, A&A, 555, 63
de Franciscis, S., Pascual-Granado, J., Suárez, J. C., et al. 2019, MNRAS, 487,4457
de Freitas, D. B., & De Medeiros, J. R. 2009, Europhys. Lett, 88, 19001
de Freitas, D. B., Leão, I. C., Lopes, C. E. F., De Medeiros, J. R., et al. 2013a, ApJL, 773, L18
de Freitas, D. B., França, G. S., Scherrer, T. M., Vilar, C. S., & Silva, R. 2013b, Europhys. Lett., 102, 39001
de Freitas, D. B., Nepomuceno, M. M. F., de Moraes Junior, P. R. V., Lopes, C. E. F., Leão, I. C. et al. 2016, ApJ, 831, 87
de Freitas, D. B., Nepomuceno, M. M. F., de Moraes Junior, P. R. V., Lopes, C. E. F., Leão, I. C. et al. 2017, ApJ, 843, 103
de Freitas, D. B., Nepomuceno, M. M. F., Alves Rios, L. D., Das Chagas, M. L. & De Medeiros, J. R., 2019a, ApJ, 880, 151
de Freitas, D. B., Nepomuceno, M. M. F., Cordeiro, J. G., Das Chagas, M. L. & De Medeiros, J. R., 2019b, MNRAS, 488, 3274
Fabrycky, D. C., Ford, E. B., Steffen, J. H., et al. 2012, ApJ, 750, 114
Gieratowski, J., Zebrowski, J., and Baranowski, R., Phys. Rev. E, 2012, 85, 021911
Gilliland, R. L., Chaplin, W. J., Jenkins, J. M., Ramsey, L. W., & Smith, J. C. 2015, AJ, 150, 133
Gu, G.-F., & Zhou, W.-X. 2010, Phys. Rev. E, 82, 011136
Henry, B., Lovell, N., Camacho, F. Nonlinear dynamics time series analysis. Akay (Ed.), Citeseer, 2001. 5, 7, 10
Hippke, M., David, T. J., Mulders, G. D., Heller, R., 2019, AJ,158, 143
Hurst, H. E. 1951, Trans. Am. Soc. Civ. Eng., 116, 770
Ihlen, E. A. F. 2012, Front. Physiology 3, 141
Jenkins, J. M., Caldwell, D. A., Chandrasekaran, H., et al. 2010b, ApJL, 713, L120
Jenkins et al., 2010a, ApJ, 713, L87
Kantelhardt, J. W., 2015, Fractal and multi-fractal time series, in Encyclopedia of Complexity and Systems Science. Springer Science & Business Media, New York
Kawaler, S. D., 1988, ApJ, 333, 236
Kinemuchi, K., Barclay, T., Fanelli, M., et al. 2012, PASP, 124, 963
Kraft R. P., 1967, ApJ, 150, 551
Krzyszczak, J.; Baranowski, P.; Zubik, M.; Kazandjiev, V.; Georgieva, V.; Sawinski, C.; Siwek, K.; Kozyra, J.; Nieróbca, A., 2018, Theor. Appl. Climatol., 137, 1811
Lanza, A. F., Rodono, M., Pagano, I., Barge, P., & Llebaria, A. 2003, A&A, 403, 1135
Lanza, A. F., Bonomo, A. S., & Rodonò, M. 2007, A&A, 464, 741
Lanza, A. F., Pagano, I., Leto, G., et al. 2009, A&A, 493, 193
Lanza, A. F. 2012, A&A, 544, A23
Lanza, A. F. 2013, A&A, 557, A31
Lanza, A. F.; Das Chagas, M. L. and De Medeiros, J.R. 2014, A&A, 564, A50
Lanza, A. F. 2016, Lecture Notes in Physics vol. 914, p.43, Berlin Springer Verlag; doi:10.1007/978-3-319-24151-7_3
Lanza, A. F., Netto, Y., Bonomo, A. S., et al. 2019, A&A, 626, A38
Lomb, N. R. 1976, Ap&SS, 39, 447
Luo, A. C. J. & Han, R. P. S., 1992, Chaos, Solitons & Fractals, 2, 335
McQuillan, A., Aigrain, S., & Mazeh, T. 2013, MNRAS, 432, 1203
Makowiec D., & Fuliński, A. 2010, Acta Phys Pol B, 41, 1025
Mathur, S., Salabert, D., Garcia, R. A., & Ceillier, T. 2014, J. Space Weather Space Clim, 4, 15
Maxted, P. F. L. 2016, A&A, 591, A111
Meunier, N., Lagrange, A.-M., Borgniet, S., et al. 2015, A&A, 583, A118. doi:10.1051/0004-6361/201525721
Panichi F., Gozdziewski K., Migaszewski C., Szuszkiewicz E.,2018, MNRAS, 478, 2480
Radick, R. R., Lockwood, G. W., Henry, G. W., et al. 2018, ApJ, 855, 75
Scargle, J. D. 1982, ApJ, 263, 835
Sanchis-Ojeda, R., Fabrycky, D. C., Winn, J. N., et al. 2012, Nature, 487, 449
Skumanich A., 1972, ApJ, 171, 565
Silva-Valio, A. & Lanza, A. F. 2011, A&A, 529, A36
Smith, J. C., Stumpe, M. C., Van Cleve, J. E., et al. 2012, PASP, 124, 1000
Stumpe, M. C., Smith, J. C., Catanzarite, J. H., et al. 2014, PASP, 126, 100
Strassmeier, K. G. 2009, A&A Rev., 17, 251
Suyal, V., Prasad, A., & Singh, H. P. 2009, Solar Phys., 260, 441
Tanna, H.J., Pathak, K.N., 2014, Astrophys. Space Sci., 350, 47
Tang, L., Lv, H., Yang, F., & Yu, L. 2015, Chaos, Solitons & Fractals, 81, 117
Thompson, S. E., Christiansen, J. L., Jenkins, J. M., et al. 2013, Kepler Data Release 23 Notes (KSCI-19063-001)
Van Cleve, J. E. & Caldwell, D. A. 2009, Kepler Instrument Handbook, KSCI-19033
Van Cleve, J. E., Jenkins, J. M., Caldwell, D. A., et al. 2010, Kepler Data Release 5 Notes, KSCI-19045-001
Walkowicz L. M., & Basri G. S., 2013, MNRAS, 436, 1883
Wang, J., Shang, P., and Cui, X., Phys. Rev. E Stat. Nonlin. Soft Matter Phys. 2014, 89, 032916
Zaqarashvili, T. V., Albekioni, M., Ballester, J. L., et al. 2021, Space Sci. Rev., 217, 15. doi:10.1007/s11214-021-00790-2
Zechmeister, M. & Kürster, M. 2009, A&A, 496, 577

Appendix A: The multifractal background

In the present appendix, we present the steps of the MFDMA algorithm according to Gu & Zhou (2010):

Step 1: Construct the sequence of cumulative sums of time series $x(t)$ over time $t = 1, 2, 3, ..., N$, assuming the datapoints are evenly spaced:

$$y(t) = \sum_{i=1}^{t} x(i), \quad t = 1, 2, 3, ..., N, \tag{A.1}$$

where N is the total number of datapoints in the time series and the index i is the time index t.

Step 2: Calculate the moving average function of Eq. (A.1) in a moving window:

$$\tilde{y}(t) = \frac{1}{n} \sum_{k=0}^{\lceil n-1 \rceil} y(t-k), \tag{A.2}$$

where n is the window size, and $\lceil (x) \rceil$ is the smallest integer that is not smaller than argument (x)[4];

Step 3: Detrend the series by removing the moving average function, $\tilde{y}(i)$, and obtain the residual sequence, $\epsilon(i)$, through:

$$\epsilon(i) = y(i) - \tilde{y}(i), \tag{A.3}$$

where $n \leq i \leq N$. We divide the residual series $\epsilon(i)$ into N_n=int$[N/n - 1]$ non-overlapping segments of the same size n, where int$[x]$ is the largest integer that is not larger than x. Each segment can be denoted by ϵ_ν so that $\epsilon_\nu(i) = \epsilon(l + i)$ where $1 \leq i \leq n$ and $l = (\nu - 1)n$;

Step 4: Calculate the root-mean-square (RMS) fluctuation function, $F_\nu(n)$, for a segment of size n:

$$F_\nu(n) = \left\{ \frac{1}{n} \sum_{i=1}^{n} \epsilon_\nu^2(i) \right\}^{\frac{1}{2}}. \tag{A.4}$$

Step 5: Generate the fluctuation function $F_q(n)$ of the qth order:

$$F_q(n) = \left\{ \frac{1}{N_n} \sum_{\nu=1}^{N_n} F_\nu^q(n) \right\}^{\frac{1}{q}}, \tag{A.5}$$

for all $q \neq 0$, where the qth-order function is the statistical moment (e.g., for q=2, we have the variance), while for $q = 0$,

$$\ln [F_0(n)] = \frac{1}{N_n} \sum_{\nu=1}^{N_n} \ln[F_\nu(n)]. \tag{A.6}$$

The scaling behaviour of $F_q(n)$ follows the relationship

$$F_q(n) \sim n^{h(q)}, \tag{A.7}$$

where $h(q)$ denotes the Holder exponent or generalized Hurst exponent. Each value of q yields a slope h and, in particular, $q = 2$ gives the classical Hurst exponent.

Step 6: Knowing $h(q)$, the multifractal scaling exponent, $\tau(q)$, can be computed:

$$\tau(q) = qh(q) - 1. \tag{A.8}$$

[4] It is possible to adopt different kinds of moving averages instead of that defined by eq. (A.2). For example, instead of considering datapoints that precede the given time t, it is possible to consider points that follow it or that are taken half before and half after the time t (see Gu & Zhou 2010).

Finally, the singularity strength function, $\alpha(q)$, and the multifractal spectrum, $f(\alpha)$, are obtained via a Legendre transform:

$$\alpha(q) = \frac{d\tau(q)}{dq} \tag{A.9}$$

and

$$f(\alpha) = q\alpha - \tau(q). \tag{A.10}$$

By definition, for a monofractal signal, h is the same for all values of q and is equal to α giving a single-value spectrum $f(\alpha) = f(h) = 1$, while for a multifractal signal, $h(q)$ is a function of q, and the multifractal spectrum is generally parabolic (see Fig. 2 from de Freitas et al. 2017).

We use the following model parameters to compute the multifractal spectrum, as recommended by Gu & Zhou (2010): $N = 30$; $q \in [-5, 5]$ with a step size of 0.2; the lower bound of segment size n, which is denoted as $n_{\min}$ and set to 10; and the upper bound of segment size n, which is denoted as $n_{\max}$ and is given by $N/10$. An estimate of the standard deviation of the Hurst exponent is provided by Kantelhardt (2015) and is < 0.03 when we consider timeseries with more than 10^4 datapoints as in our case.

Appendix A.1: Multifractal indicators

We use a set of four multifractal indicators that can be extracted from the quantities defined in Eqs. A.8, A.9 and A.10, in particular from the multifractal spectrum $f(\alpha)$ as illustrated in Fig. 2 of de Freitas et al. (2017). In this paper, we refer to this same figure to describe the shape of the multifractal spectrum. Here, we show a list of the main indicators:

Parameter α_0:

The α_0 parameter is the value of α corresponding the maximum of the multifractal spectrum $f(\alpha)$. It delivers information about the structure of the process producing the fluctuations, with a high value indicating that it is less correlated and has a fine structure (Krzyszczak et al. 2018). In addition, this parameter is strongly affected by signal variability. This is evidenced when one investigates the different sources of multifractality that are present in an astrophysical signal (see Sect. 5.2).

Singularity parameter $\Delta f_{\min}(\alpha)$:

The parameter $\Delta f_{\min}(\alpha)$ characterizes the broadness, which is defined as the difference $f(\alpha_{\max}) - f(\alpha_{\min})$ of the singularity spectrum. This difference provides an estimate of the spread in changes in fractal patterns. Consequently, if $\Delta f_{\min}(\alpha)$ is positive, the left-hand side of the spectrum is less deep, while a negative value indicates that this side is deeper. On the other hand, when $\Delta f_{\min}(\alpha)$ is null, the depths of the tails are the same on both sides. As quoted by Ihlen (2012), larger fluctuations ($q > 0$) imply that the singularities are stronger, whereas the smaller fluctuations ($q < 0$) indicate that the singularities are weaker (cf. Tanna & Pathak 2014). In other words, multifractal spectra that have a longer right tail than the left one reveal that the structure of the time series is more regular and less dominated by extreme (maximal) values and, therefore, the parameter $\Delta f_{\min}(\alpha)$ can be a useful way to estimate the impact of noise in the periodic signal.

Degree of asymmetry (A):

This index is defined as the ratio:

$$A = \frac{\alpha_{\max} - \alpha_0}{\alpha_0 - \alpha_{\min}}, \tag{A.11}$$

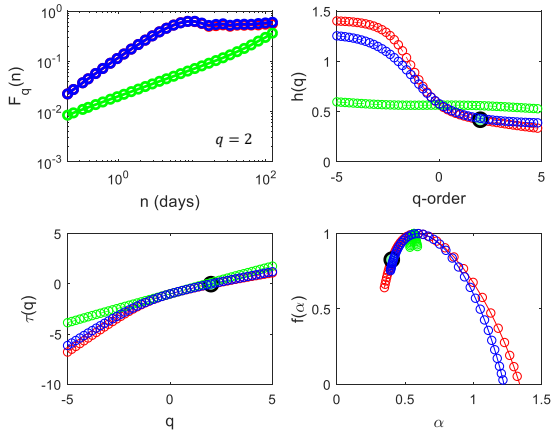

Fig. A.1. Multifractal analysis for PDC time series following steps 5 and 6 presented in Section 4. *Top panel*: The original (in red), the shuffled (green) and phase randomized (blue) data are based on the procedure mentioned in Section 4. *Left top*: the multifractal fluctuation function $F_q(n)$ obtained from MFDMA method for only $q = 2$, indicated henceforth as a big circle. *Right top*: q-order Hurst exponent ($h(q)$) as a function of q-parameter. This panel shows the truncation originated from the leveling of the $h(q)$ for positive q's. *Left bottom*: comparison of the multifractal scaling exponent $\tau(q)$ of three data. In this panel is possible to identify a crossover in $q \sim -1$. *Right bottom*: multifractal spectrum $f(\alpha)$ of three time series, respectively.

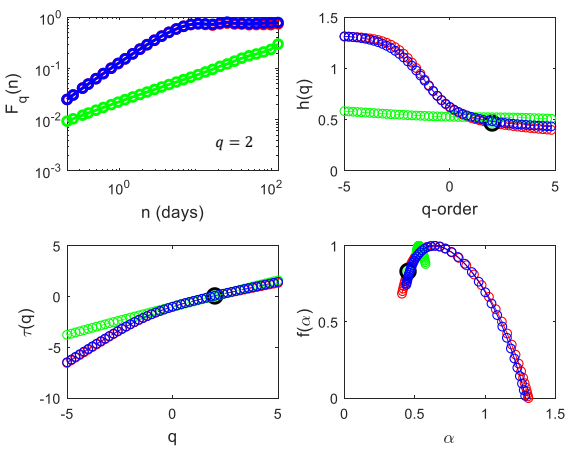

Fig. A.2. Idem figure A.1 for SAP time series.

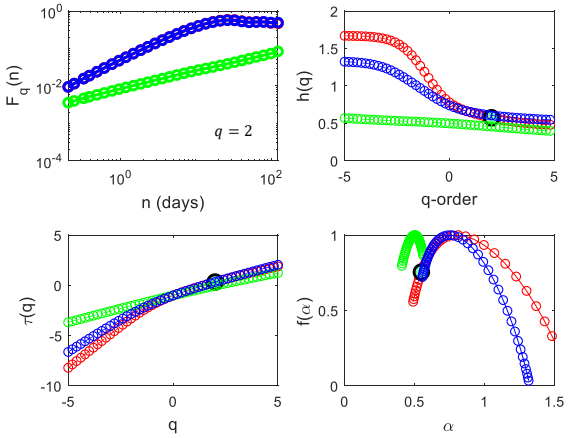

Fig. A.3. Idem figure A.1 for RTS data.

where α_0 is the value of α where $f(\alpha)$ is maximal, while $\alpha_{\min}$ and $\alpha_{\max}$ are the minimum and maximum values of the singularity exponent α as defined by eq. A.9, respectively. The value of A indicates one of three possible skewness of the singularity spectrum: right-skewed ($A > 1$), left-skewed ($0 < A < 1$) or symmetric ($A = 1$).

Degree of multifractality ($\Delta\alpha$):

This index represents the measure of the interval:

$$\Delta\alpha = \alpha_{\max} - \alpha_{\min}, \tag{A.12}$$

where $\alpha_{\max}$ and $\alpha_{\min}$ are defined above. A low value of $\Delta\alpha$ indicates that the time series is close to fractal with the multifractal strength being higher when $\Delta\alpha$ increases (de Freitas & De Medeiros 2009; de Freitas et al. 2017). As mentioned by de Freitas et al. (2016), larger values of $\Delta\alpha$ denote more complex fluctuations, whereas smaller values indicate that the spectrum tends towards the monofractal limit. According to Makowiec & Fuliński (2010), if $\Delta\alpha$ is less than 0.05 a monofractal behaviour of the spectrum should be assumed because of the intrinsic precision in deriving such a parameter from a statistics based on a number of datapoints that is in any case limited.

Appendix A.2: Results based on the standard multifractal approach

First, we calculate the MFDMA fluctuation functions $F_q(n)$ as a function of window size n (in days) for the three time series PDC, SAP, RTS. The scale parameter n is varied from 10 to $N/10$, and the exponent q is varied from -5 to 5 in steps of 0.2. The scaling pattern of $F_q(n)$ of original data (red lines) for $q = 2$ is shown in the top left panels of Figs. A.1, A.2 and A.3. We repeat the analysis for a set of 200 randomly shuffled series as well as for 200 phase-randomized series (blue and green lines, respectively).

For PDC, SAP and RTS from Kepler-30, the standard multifractal characterization was performed following the procedures described above and also for the series obtained from surrogates of the original data sets. For all of the timeseries, the above four multifractal indicators together with the Hurst exponent H were obtained, and their values are shown in Table 1 where the parameters associated with the original timeseries are denoted with an (O) superscript, while those associated with the shuffled and the phase-randomized series with an (S) or (P) superscripts, respectively.

For all the series and q-domains, the multifractality due to correlation is stronger than that due to the non-Gaussianity of the distribution of the fluctuations with fat tails as indicated by "1" and the positive values of $\Delta f^{O}_{\min}(\alpha)$. This value does not imply that there are only long-term correlations in fluctuations, but it implies that non-linearities due to fat-tailed distributions are very weak. As a consequence, a time-independent structure with $h(q) \approx 0.5$ is shown in the shuffled time series (see Figs. A.1, A.2 and A.3). After shuffling, all time series exhibit a smaller degree of multifractality than the original one. This result can be emphasized by the multifractal spectra (green curves from right top panels). In general, this analysis is not conclusive for explaining the source of this behaviour. In this case, it is necessary to verify the behaviour of $\tau(q)$. As illustrated by Fig. A.4, there is a strong

Table A.1. The multifractal indicators extracted from the standard MFDMA method for PDC, SAP and RTS. The results are summarized considering the Original (O), Shuffled (S) and Phase randomized (P) data. From left to right, we have: the columns $q < 0$ and $q > 0$ (see Section 4.2 for further details), the multifractality due to long-term correlation is stronger than that due to non-linearity; singularity parameter; parameter α_0; global Hurst exponent; degree of multifractality and; degree of asymmetry.

	$q<0$	$q>0$	$\Delta f^O_{min}(\alpha)$	α_0^O	α_0^S	α_0^P	H_O	H_S	H_P	$\Delta\alpha_O$	$\Delta\alpha_S$	$\Delta\alpha_P$	A_O	A_S	A_P
PDC	1	1	0.59	0.59	0.56	0.60	0.42	0.53	0.44	0.97	0.12	0.86	2.95	1.13	3.20
SAP	1	1	0.67	0.64	0.52	0.66	0.47	0.55	0.47	0.90	0.06	0.92	2.88	1.79	2.64
RTS	1	1	0.52	0.81	0.51	0.75	0.58	0.49	0.61	1.12	0.13	0.73	2.47	1.83	3.50

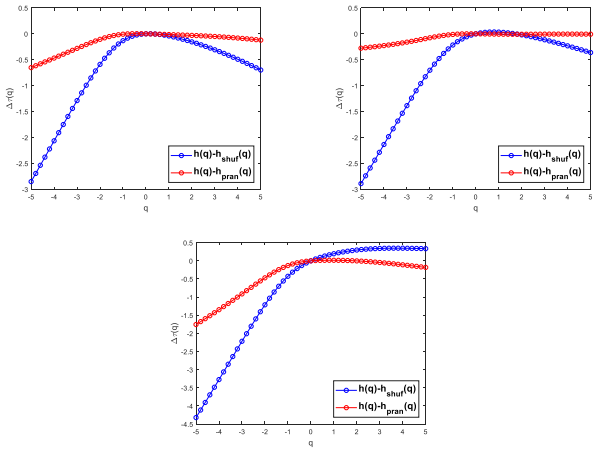

Fig. A.4. Deviations of scaling exponent for (top left) PDC, (top right) SAP and (bottom) RTS data.

dependence of $h(q) - h_{shuf}(q)$ on q, which is clearest for $q < 0$, where a deeper right tail occurs in multifractal spectra (see right bottom panels from Figs. A.1, A.2 and A.3). In contrast, the dependence on q can be neglected for the phase-randomized data, except for $q < 0$ in PDC and RTS data as illustrated by Fig. A.4. Thereby, the two sources of multifractalities appear in $q < 0$, the domain where the rotational modulation occurs. Basically, the correlations and non-linearities are negligible for $q > 0$, where the strong fluctuations due to the noise (correlated or not) appear.

Because the presence of rotational modulation and noise can affect the multifractal indicators, we decided to investigate the changes of the multifractal spectrum and compare the indicators calculated from the original series with those obtained from the surrogate series. Consequently, it is possible to find the source(s) that affect the values of α_0, H, $\Delta\alpha$ and A following the behaviour of their calculated values from the surrogate series.

Firstly, the relation between the values of α_0 in the three time series show a clear difference among them. It is interesting to note that SAP data have larger α_0^O values than the PDC time series, which means that in PDC data the fluctuations governing the rotational modulation are more correlated and have a less fine structure (a structure more regular in appearance) compared to the fluctuations of the SAP data. For RTS data, the fluctuations are even less correlated and have a more fine structure (a structure less regular in appearance) compared to the processes governing the PDC and SAP data. Secondly, the values of H for the surrogate data indicate that shuffling the data destroys the correlations, and therefore H tends to 0.5, whereas the phase-randomized data recover a value very close to that found for the original series.

In contrast, the degree of multifractality $\Delta\alpha$ changes more broadly. Because this parameter is connected to the richness of the data structure, we highlight that the $\Delta\alpha$ for the original time series of RTS indicates such data may promote some values of the fluctuations, making the signal structure richer. Nevertheless, there is an important detail. As $\Delta f^O_{\min}(\alpha)$ is the smallest value, the broadness of $\Delta\alpha$ is a mixing between strong and weak fluctuations, and therefore the noise has an important effect over the data, as can be emphasized by the small values of $\Delta\alpha_S$. However, following the criterion of Makowiec & Fuliński (2010), the shuffling process does not reduce the series to a monofractal.

It is possible to observe a dissimilarity for the asymmetry parameter A_O among the time series for both the original and the surrogate data. As shown in Figs. A.1, A.2 and A.3, and Table A.1, it is interesting that generally the spectra are rather right-skewed (which suggests that fine structures are more frequent) or tend to be symmetrical in shape. However, the extreme events become stronger for the RTS data, as the left side of the spectrum of this series is deeper than those from PDC and SAP data.

In conclusion, it is interesting to address a comparison of the parameters of the multifractal spectra between the two time series, namely PDC and SAP. It allows us to address the question of whether the MFDMA method can be applied as an indicator of the changes in the dynamics of fluctuations and, therefore, of processes occurring in the stellar atmosphere from which the stellar flux comes. It can be observed that the values of α_0 change only slightly and are greater in the SAP data. On the other hand, the degree of multifractality is more developed in the PDC data, whereas the asymmetry for SAP time series is slightly more positive. Some differences between both time series can be also seen when analysing the absolute differences of Hurst exponents for the original and shuffled data or original and surrogates (see Fig. A.4). Even though we do not see a change between both time series, it is noticed that the source of multifractality due to the contribution of long-range correlations is dominant.

Appendix B: Fluctuation functions for a sinusoidal signal

We consider a noiseless purely sinusoidal signal with constant amplitude and phase to study how the fluctuation functions computed with the MFDMA behave under the effect of a sinusoidal modulation. Suyal, Prasad & Singh (2009) investigated a similar case using a re-scaled range analysis, the so-called R/S method (e.g., Kantelhardt 2015), to evaluate the fluctuations function, but did not discuss the case of the MFDMA method. In our case, we see that the $F_q(n)$ fluctuation functions, plotted as a function of n (see Fig B.1) show a linear trend followed by an oscillating phase, a behaviour similar to that shown in Figures 13, 14 and 15. Other factors can lead to deviations from this ideal behaviour, such as noise and/or the superposition of other low-amplitude periodicities. The combination of these contributions should make the simulated time series closer to the observed ones.

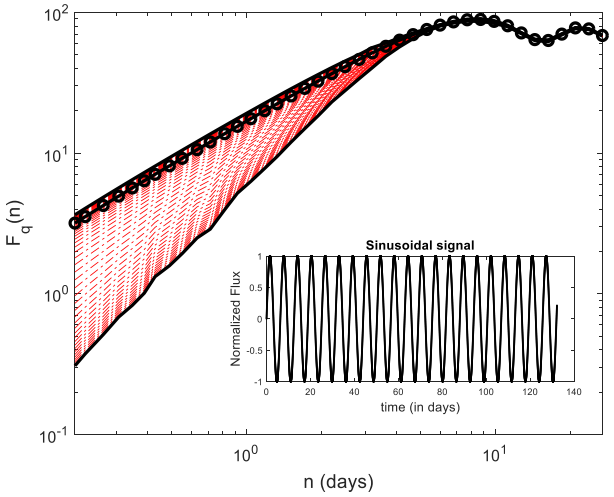

Fig. B.1. The log-log plot of fluctuation functions $F_q(n)$ vs. n for a sinusoidal time series (shown in the subplot) with period of ∼ 6.3 days.

Appendix C: Spot modelling

To map the photosphere of Kepler-30, we subdivide it into 200 surface elements of side 18° × 18° and assume that in each element there are dark spots with a filling factor f, solar-like faculae with a filling factor Qf, and unperturbed photosphere with a filling factor $1 - (Q + 1)f$, where Q is the ratio of the area of the faculae to that of the spots in each element. For simplicity, Q is assumed constant in our model.

The contrast of the dark spots is defined as $c_s \equiv I_{spot}/I_u$, where I_{spot} is the brightness of the spotted photosphere and I_u that of the unperturbed photosphere; c_s is assumed to be constant. In our case, $c_s = 0.85$ in the Kepler passband has been derived from the occulted spots producing characteristic bumps along the photometric profiles of the transits (Sanchis-Ojeda et al. 2012).

The facular contrast is assumed to be zero at the centre of the stellar disc and maximum at the limb as we observe in the Sun, that is, $c_f = c_{f0}(1 - \mu)$, where $c_{f0} = 1.115$ is the contrast at the limb and $\mu \equiv \cos\psi$, where ψ is the angle between the normal to the surface at a given point and the line of sight. Note that the effect of the faculae is parametrized by the product Qc_{f0}, thus, their contrast and their area ratio are not independent parameters (cf. Lanza 2016). Therefore, we keep c_{f0} constant and very Q (see below).

The limb-darkening of the unperturbed photosphere is expressed by means of a quadratic law:

$$I_u(\mu) \propto a_p + b_p\mu + c_p\mu^2, \tag{C.1}$$

where a_p, b_p, and c_p are derived from the limb-darkening coefficients given by Sanchis-Ojeda et al. (2012).

Our model assumes that the distribution of the filling factor f over the surface of the star is fixed while fitting the light curve. Because spots are evolving, this means that we cannot apply our model to fit the entire photometric time series, but we must fit individual intervals of duration Δt_f over which the hypothesis of a fixed spot pattern is satisfied. In stars with a slowly evolving spot pattern, the best choice is to take Δt_f equal to the mean rotation period. This will give a uniform sampling of all the longitudes along each individual rotation (Lanza, Bonomo & Rodonò 2007).

Unfortunately, this is not the case for Kepler-30 because its starspots evolve quite rapidly, thus imposing a shorter time interval to adequately fit its light modulation. Following the method applied in previous modelling of other CoRoT or Kepler targets (e.g. Lanza et al. 2019), we derive the best values of Δt_f and Q by applying a simplified spot model assuming only three discrete spots plus a uniform background (Lanza et al. 2003).

The value of Δt_f is derived by considering that in general the chi square of the best fit to the entire light curve decreases with the decrease of Δt_f. However, the reduction of the chi square becomes small when Δt_f becomes equal to or shorter than the typical timescale of spot evolution. Therefore, we progressively decrease Δt_f until the decrease of the chi square is no longer significant according to a statistical test based on the Fisher-Snedecor statistics and in this way we select the optimal Δt_f. Note that for each trial value of Δt_f, we compute models with different values of Q spanning a large interval to select the minimum of the chi square. This is made possible by the relatively short CPU time required to compute the best fit with the three-spot model in comparison to the full model assuming a continuous spot distribution.

The value of Q minimizing the chi square for the optimal value of Δt_f is adopted for our spot modelling. In the case of Kepler-30, we find that the optimal $\Delta t_f = 11.963$ days, that is, ∼ 0.75 of the mean rotation period, while $Q = 0.5$, that is much smaller than the value adopted for the spot modelling of the Sun as a star by Lanza, Bonomo & Rodonò (2007), where $Q_\odot = 9.0$. This is in agrement with the finding that dark spots dominate the optical light modulation of stars significantly more active than the Sun as is the case for Kepler-30 (cf. Radick et al. 2018).

The inclination of the stellar spin to the line of sight is derived by assuming that the stellar spin is normal to the orbital plane of the planet Kepler-30c that is the largest body in the system after the star. Nevertheless, the orbits of the other planets are virtually coplanar, so this is equivalent to assuming that the stellar spin is perpendicular to the mean plane of the planetary orbits. Note that the possibility of constraining the inclination of the stellar spin reduces the degeneracies of our spot modelling and is made possible by the presence of transiting planets around the star.

The parameters adopted in our spot modelling are listed in Table C.1. The mass and the radius of the star together with its rotation period are used to compute the surface gravity as a function of the latitude to account for the effects of the gravity darkening. They are of the order of 10^{-6} in relative flux units and do not affect our solution.

The effects of the uncertainties in the model parameters on the spot modelling have been discussed in detail by Lanza et al. (2009) e Lanza et al. (2019). They are negligible for our application because we are mainly interested in the typical timescales of starspot evolution rather than on the absolute values of the spotted area or of the surface differential rotation.

By minimizing the chi square of the fit to the light curve with our continuous spot model, we can find a unique spot map for Kepler-30, but such a map is unstable in the sense that a small change in the data produces a large change in the map because most of the map details come from fitting the photometric noise and the evolution of small spots along each Δt_f time interval. Regularization can provide a unique map by reducing the fitting of the noise and of the small fluctuations and therefore the consequent instability. This is achieved by imposing a priori assumptions on the spot map that are coded into a regularization functional $S(\mathbf{f})$ that depends on the vector $\mathbf{f}$, the components of

Parameter		Reference
Mass ($M_\odot$)	0.99	1
Radius ($R_\odot$)	0.95	1
$P_{\rm rot}$	16.0	1
i (deg)	89.68	2
$c_{\rm s}$	0.85	1
$a_{\rm p}$	0.22	1
$b_{\rm p}$	1.18	1
$c_{\rm p}$	-0.40	1
Q	0.5	2
$\Delta t_{\rm f}$ (d)	11.963	2

Table C.1. Parameters adopted in the spot modelling of Kepler-30. References: 1: Sanchis-Ojeda et al. (2012); 2: present work

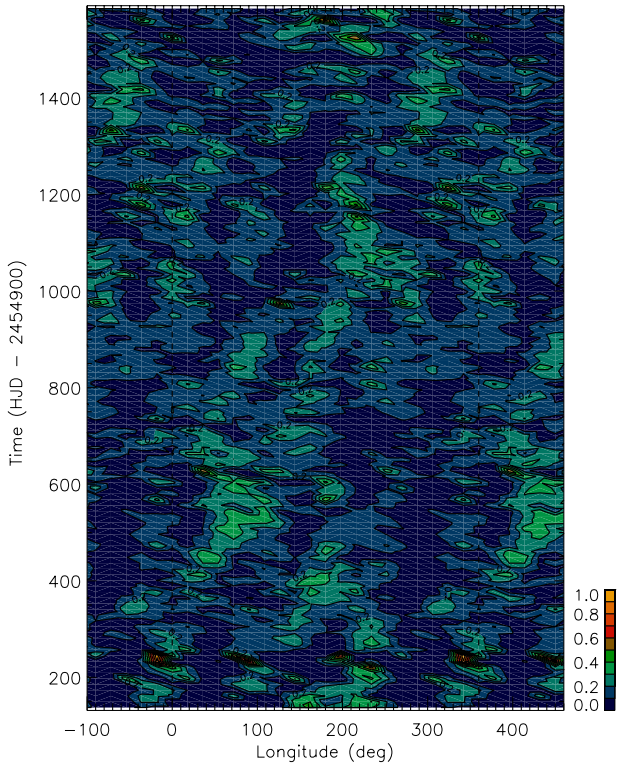

Fig. C.1. Distribution of the spot filling factor vs. the longitude and time for the ME regularized spot model of the SAP light curve of Kepler-30. The minimum of the filling factor corresponds to dark blue regions, while the maximum is rendered in orange (see the colour scale close to the lower right corner of the plot). Note that the longitude scale of the horizontal axis is extended beyond the $[0°, 360°]$ interval to better follow the migration of the starspots.

which are the filling factors of the 200 surface elements of our map (see eq. (3.25) in Lanza 2016, for the expression of S).

In the case of a regularized best fit, instead of minimizing the chi square χ^2 between the observed and the modelled fluxes, we minimize a linear combination of the χ^2 and the regularizing functional S, viz:

$$Z(\mathbf{f}) = \chi^2(\mathbf{f}) - \lambda_{\rm ME} S(\mathbf{f}), \tag{C.2}$$

where $\lambda_{\rm ME} > 0$ is a Lagrangian multiplier that rules the level of regularization. When $\lambda_{\rm ME}$ is zero, we get the unregularized

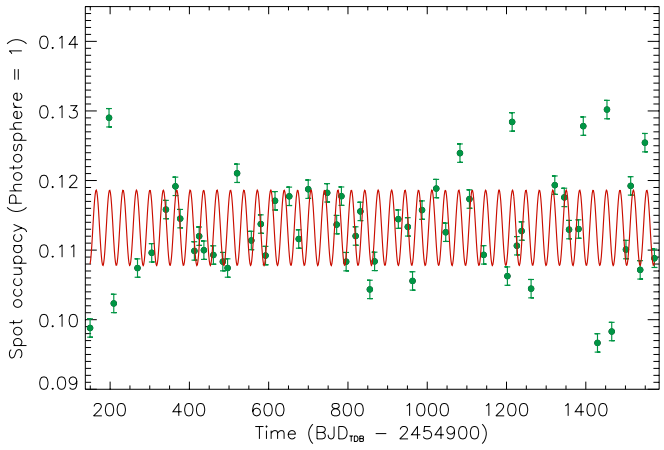

Fig. C.2. The total spotted area on Kepler-30 as derived from the spot modelling of the SAP light curve vs. the time (green dots). A sinusoid with a period of 33.878 days corresponding to the maximum of the GLS periodogram is overplotted (red solid line).

model that has the minimum χ^2 and residuals that are symmetrically distributed around a zero mean $\mu_{\rm res}$. When we increase $\lambda_{\rm ME}$, we increase the χ^2 above its minimum and the mean of the residuals is no longer zero because the ME regularization drives the map towards an unspotted photosphere, thus making the residuals systematically negative. In other words, the functional S is designed to be maximal when the star is unspotted, so that, by introducing the regularization, we drive the map towards that of an unspotted star.

The criterion to fix the Lagrangian multiplier is crucial to decide when the process of regularization has to be stopped to avoid that the χ^2 becomes too large and the fit unacceptable. As in the case of similar stars with a photon shot noise of the single datapoint of the order of $\sim 1\%$ of the amplitude of the flux modulation produced by starspots, we iteratively increase $\lambda_{\rm ME}$ until the absolute value of the mean of the residuals $|\mu_{\rm res}|$ becomes equal to the standard error $\epsilon_{\rm st}$ of the datapoints in the fitted interval of duration $\Delta t_{\rm f}$. The standard error is computed from the standard deviation σ_0 of the residuals of the unregularized best fit and the number of datapoints M in each interval $\Delta t_{\rm f}$ as $\epsilon_{\rm st} = \sigma_0/\sqrt{M}$. For each interval $\Delta t_{\rm f}$, we determine $\lambda_{\rm ME}$ by enforcing the equality $|\mu_{\rm res}| = \epsilon_{\rm st}$ within 5% both for the fit of the PDC and the SAP light curves.

The unregularized best fit of the SAP light curve obtained with our model is very similar to that of the PDC timeseries and is not shown here. The regularized spot map is shown in Fig. C.1 and is similar to that obtained with the PDC light curve. The SAP light curve shows a range of amplitudes of the light modulation larger than the PDC light curve because the Kepler pipeline tends to reduce the variability at timescales longer than 15 – 20 days. As a consequence, the SAP spot map shows a wider distribution of the filling factor than the PDC map, but the location of the spots and their evolution are very similar to those shown in the PDC map.

The total spotted area as derived by the ME regularized spot model of the SAP light curve is plotted in Fig. C.2 as a function of the time. As in the case of the PDC light curve, only the intervals $\Delta t_{\rm f}$ with datapoints having a sufficiently uniform distribution are considered to avoid systematic effects produced by the ME regularization (see Sect. 7.2). A modulation with a period of

$\sim$ 33.9 days is apparent as indicated by the sinusoid superposed to the plot.